Rapid Communications

Counterflowing edge current and its equilibration in quantum Hall devices with sharp edge potential: Roles of incompressible strips and contact configuration

T. Akiho, H. Irie, K. Onomitsu, and K. Muraki
NTT Basic Research Laboratories, NTT Corporation, 3-1 Morinosato-Wakamiya, Atsugi 243-0198, Japan

(Received 5 February 2019; revised manuscript received 8 March 2019; published 27 March 2019)

We report the observation of counterflowing edge current in InAs quantum wells which leads to the breakdown of quantum Hall (QH) effects at high magnetic fields. Counterflowing edge channels arise from the Fermi-level pinning of InAs and the resultant sharp edge potential with downward bending. By measuring the counterflow conductance for varying edge lengths, we determine the effective number $\langle N_C \rangle$ of counterflowing modes and their equilibration length λ_{eq} at a bulk integer filling factor $\nu = 1$–4. λ_{eq} increased exponentially with magnetic field B, reaching 200 μm for $\nu = 4$ at $B \geqslant 7.6$ T. Our data reveal important roles of the innermost incompressible strip with even filling in determining $\langle N_C \rangle$ and λ_{eq} and the impact of the contact configuration on the QH effect breakdown. Our results show that counterflowing edge channels manifest as transport anomalies only at high fields and in short edges. This in turn suggests that, even in the integer QH regime, the actual microscopic structure of the edge states can differ from that anticipated from macroscopic transport measurements, which is relevant to various systems including atomic-layer materials.

DOI: 10.1103/PhysRevB.99.121303

Understanding and controlling the electronic states at the edge of a two-dimensional system are becoming increasingly important. This is particularly true for topologically nontrivial systems, such as quantum Hall (QH) [1–3] and quantum spin Hall [4,5] systems, where gapless edge states with distinct properties appear. Recent theories [6–10] predict that, by coupling their edge states to superconductors, QH as well as quantum spin Hall systems can be exploited to engineer exotic quasiparticles with non-Abelian statistics, a building block for robust quantum computation [11,12]. Semiconductor heterostructures comprising InAs, which can form transparent junctions with superconductors [13–15], are promising for such purposes. Theory further predicts that certain fractional QH edge states coupled through a superconductor may harbor even more exotic quasiparticles that would allow for universal topological quantum computation [6–10]. Motivated by these predictions, recently, the quality of InAs-based heterostructures has been improved significantly [16,17], which has led to the observation of a fractional QH effect [18].

In standard GaAs-based heterostructures, the edge potential is bent upward by the Fermi-level pinning in the band gap so that the electron density decreases monotonically toward the edge [1,19]. This forms the basis for the common situation in QH systems where all edge channels have the same chirality, flowing in the same direction set by the magnetic field [20]. In contrast, in InAs the surface pinning occurs in the conduction band [21,22], which implies that in heterostructures the edge potential is bent downward so the electron density increases near the edge. While this is advantageous for superconducting junctions, it gives rise to trivial edge conduction with no topological origin at zero magnetic field [15,23–26]. In a quantizing magnetic field, this suggests that the Fermi level can cross Landau levels extra times (see the inset in Fig. 1), where additional sets of edge channels form [27]. Since the direction of the electron drift velocity is determined by the sign of the potential gradient, the additional edge channels carry current in the forward and counterflow directions. As recently revealed in graphene [28], a similar situation can also occur in a gated device due to electric field focusing near the edge [29].

Counterflowing edge channels were first conceived by van Wees *et al.* [27], who observed in their InAs quantum well that QH effects collapsed when a negative gate voltage below a certain threshold (~ -0.4 V) was applied. The results were then explained using the Landauer-Büttiker model [3], taking into account the scattering between forward and counterflowing edge channels, which indicated a typical equilibration length in excess of 200 μm. However, it remains unknown what determines the equilibration length and how it depends on the parameters such as the magnetic field and filling factor. In this Rapid Communication, we address these issues by systematically studying QH edge transport in InAs quantum wells using gated Hall-bar devices with only well-defined edges. We directly detect the upstream charge current using a three-terminal setup, which allows us to determine the effective number of counterflowing modes and their equilibration length. Our data reveal important roles of the innermost incompressible strip with even filling and the impact of the contact configuration for the counterflowing edge channels to manifest in transport. Our results provide insights into the microscopic details of QH edge states, which will be useful for understanding edge transport in various systems including atomic-layer materials and in superconducting junctions, not only in the QH but also in the quantum spin Hall setups.

The heterostructure studied was grown by molecular beam epitaxy on an *n*-type GaSb (001) substrate. The layer structure comprises a 20-nm-thick InAs quantum well sandwiched between $Al_{0.7}Ga_{0.3}Sb$ barriers, with no intentional doping to supply carriers. The center of the well is located 65 nm below the surface of the 5-nm-thick GaSb cap. The heterostructure

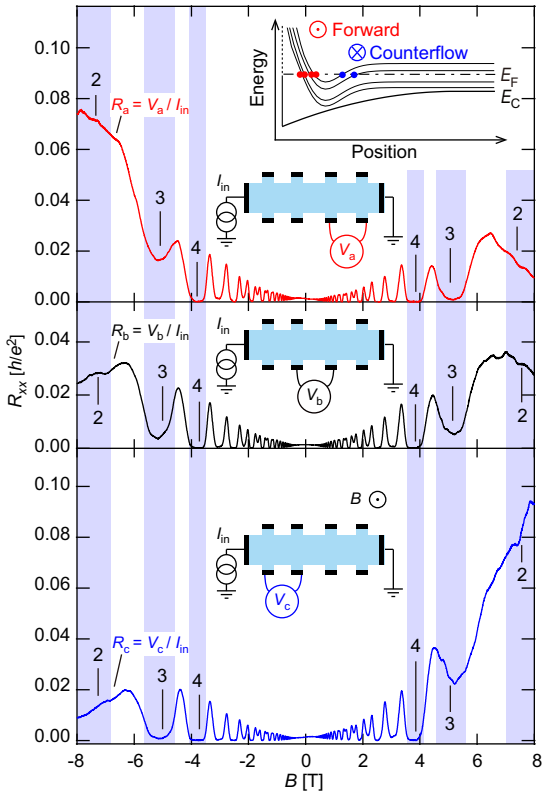

FIG. 1. Probe-position dependence of R_{xx} vs B of sample A. The insets show the contact configuration for each measurement. Inset of the upper panel: Schematic diagram of the conduction band edge (E_C) and Landau-level dispersion in the presence of Fermi-level pinning in the conduction band at the edge. Edge channels are formed when the Fermi level (E_F) crosses the Landau levels.

was processed into 50-μm-wide Hall bars as shown in the inset of Fig. 1 by wet etching [30]. We fabricated devices with ten Ti/Au Ohmic electrodes and a Ti/Au gate on an atomic-layer-deposited 40-nm-thick Al_2O_3 insulator. The gate covers all the mesa edges and their interface with Ohmic contacts, so that all the edges are defined in the same way. The sample had a sheet electron density of $n = 3.65 \times 10^{15}$ m^{-2} and a low-temperature mobility of 50 m^2/V s. We used two samples fabricated from the same wafer, sample A with all edges having the same length of $L_{edge} = 60$ μm and sample B with varying L_{edge} (=30−280 μm). Measurements were done at 1.5 K using a standard lock-in technique with a frequency of 33 Hz and current I_{in} of 10 nA. The virtual-ground input of the lock-in amplifier was used to measure the current.

We first present results for sample A. Figure 1 shows the magnetic field (B) dependence of the longitudinal resistance (R_{xx}) at a front gate voltage $V_{FG} = 0$ V, measured using different pairs of voltage probes on the lower edge of the sample. At $|B| \leqslant 4$ T, we observe normal behavior—Shubnikov–de Haas oscillations and a well-developed QH effect at a Landau-level filling factor $\nu = 4$—for all configurations ($\nu = nh/eB$ with e the elementary charge and h Planck's constant). In contrast, anomalous behavior is seen at $|B| > 4$ T, where the QH effects expected at $\nu = 3$ and 2 are not fully developed or completely missing, as seen by the nonvanishing R_{xx}. Interestingly, the values of the finite R_{xx} at $\nu = 3$ and 2 systematically depend on the field direction and probe position. At $\nu = 2$, R_{xx} measured with the lower-right probes (R_a) is much higher for $B < 0$ than for $B > 0$. Opposite behavior is seen for R_{xx} measured with the lower-left probes (R_c), which is much higher for $B > 0$. The lower-middle probes (R_b) give intermediate values nearly symmetric for both field directions. Although not shown, measurements using the probes on the upper edge confirm similar behavior, but with the probe-position dependence 180° rotated around the sample normal. (Additional measurements with $I_{in} = 100$ nA confirmed that there was no significant current dependence.) We show below that this chiral breakdown behavior of the QH effect can be explained by the Landauer-Büttiker model that takes into account the scattering between forward and counterflowing edge channels.

We demonstrate the existence of counterflowing charge current using the three-terminal measurements as illustrated in Fig. 2(a), which in turn allowed us to directly determine the number of counterflowing modes (N_C) and their transmission probability (T_C) for individual edges. In order to examine the L_{edge} dependence of T_C, we used sample B with varying L_{edge} (=30−280 μm). A magnetic field was applied in the direction so that the chirality of the edge channels was clockwise. With this three-terminal setup, we detected charge current I_{cntr} at the probe located on the upstream of the electrode from which I_{in} (∼10 nA) was driven, in addition to normal forward current I_{fwd} measured on its downstream. To check the conduction through the bulk, we also monitored current I_{opp} on the opposite side of the Hall bar. In the QH regime, where the current cannot flow through the bulk, the chirality requires $I_{fwd} = I_{in}$ and $I_{cntr} = 0$. As shown in Fig. 2(b), we observe that this holds only at $B = 2$–4 T. At $B > 4$ T, I_{fwd} is seen to be noticeably lower than I_{in} at fields where I_{opp} is vanishing, accompanied by a significant increase in I_{cntr}. This observation of upstream charge current in the QH regime provides direct evidence for the existence of counterflowing edge channels.

Using the voltage V_{in} applied to drive I_{in} and measured currents I_{fwd} and I_{cntr} in the QH regime, we define the conductance in the forward and counterflow directions as $g_F^{(i)} = (I_{fwd}/V_{in})/G_0$ and $g_C^{(i-1)} = (I_{cntr}/V_{in})/G_0$ for the edges on the downstream and upstream labeled i and $i-1$, respectively, in units of conductance quantum $G_0 = e^2/h$. In the Landauer-Büttiker model [3,27], g_C can be expressed as $g_C^{(i-1)} = N_C T_C^{(i-1)}$, where $T_C^{(i-1)}$ is the transmission probability of the counterflowing mode of the edge on the upstream labeled $i-1$. Note that there are $\nu + N_C$ forward edge channels in the presence of N_C counterflowing edge channels. Detailed balance requires $g_F^{(i)} = \nu + g_C^{(i)}$ for each edge [31]. In what follows, we therefore show only results for g_C. We repeated similar three-terminal measurements using the same sample while sequentially changing the injector and detector contacts, which allowed us to evaluate g_C for different edges. Figure 2(c) shows g_C for different L_{edge}, obtained while sweeping V_{FG} at a fixed magnetic field of 6 T. The top axis shows the bulk filling factor determined from the low-field Shubnikov–de Haas oscillations and Hall measurements at each V_{FG}. We note that g_C oscillates with V_{FG}, but with the positions of the minima shifted from the bulk integer filling to lower V_{FG} [32].

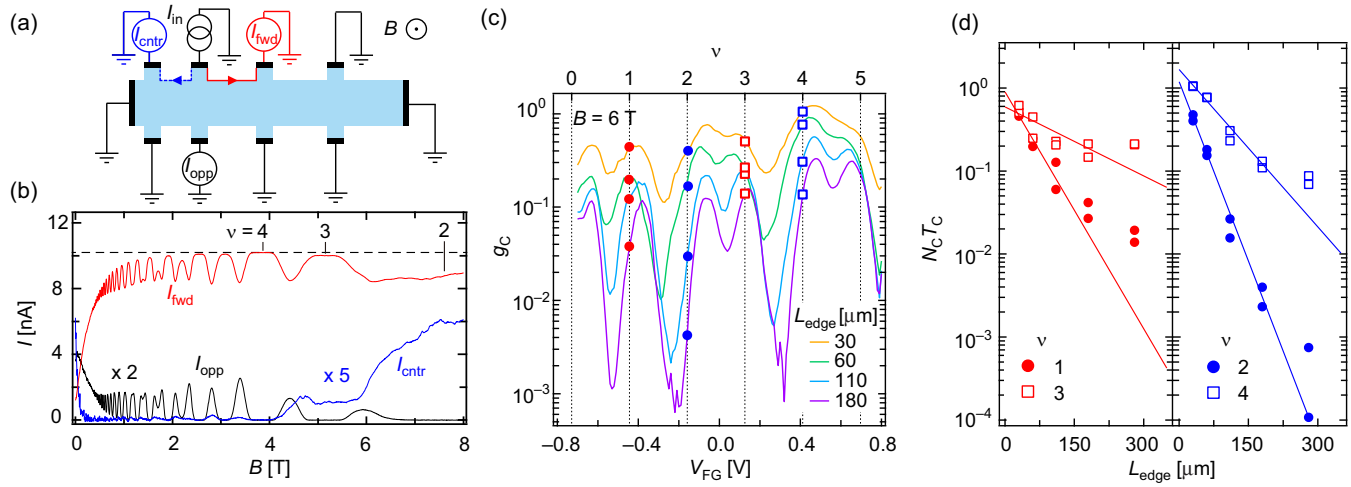

FIG. 2. (a) Schematic of the three-terminal measurement detecting upstream counterflowing current I_{cntr} in addition to normal forward current I_{fwd} (shown by the blue and red arrows, respectively). Current I_{opp} at the opposite side of the Hall bar was also monitored as a measure of bulk conduction. (b) Magnetic field dependence of I_{fwd}, I_{cntr}, and I_{opp}, measured in sample B at $V_{FG} = 0$ V using the configuration shown in (a). (c) V_{FG} dependence of the normalized counterflow conductance g_C ($\propto I_{cntr}$) for different edge length (L_{edge}) at $B = 6$ T (see main text for details). The top axis indicates the bulk filling factor estimated from the low-field Shubnikov–de Haas oscillations and Hall measurements at each V_{FG}. (d) L_{edge} dependence of $N_C T_C$ ($=g_C$) for $\nu = 1$–4 extracted from the data in (c). Solid lines are fitting using a single exponential function.

As Fig. 2(c) shows, g_C decreases with increasing L_{edge} for all V_{FG}. In the following, we restrict our analysis to the g_C values at integer bulk filling [shown by symbols in Fig. 2(c)], where we confirmed the absence of bulk conduction. In Fig. 2(d), we plot $N_C T_C$ ($=g_C$) at 6 T as a function of L_{edge} for $\nu = 1$–4. The data were then fitted with a single exponential function $N_C T_C = A \exp(-L_{edge}/\lambda_{eq})$ using A and λ_{eq} as fitting parameters. As $T_C \to 1$ is expected for $L_{edge} \to 0$, we see that $A = N_C$. We therefore use $\langle N_C \rangle$ instead of A to represent the effective number of counterflowing modes deduced from the fitting. For $\nu = 4$, we obtain $\langle N_C \rangle = 1.67$ and $\lambda_{eq} = 70$ μm at $B = 6$ T.

We performed similar measurements and analysis for a range of magnetic fields ($B = 4$–8 T). The results are summarized in Fig. 3, where λ_{eq} and $\langle N_C \rangle$ obtained for $\nu = 1$–4 are plotted as a function of V_{FG}. For all ν, λ_{eq} monotonically increases with increasing V_{FG} [Fig. 3(a)] and hence B (inset) [33]. This suggests that the distance between the forward and counterflowing edge channels increases with B, which reduces the scattering between them. At high fields, λ_{eq} for $\nu = 3$ and 4 reaches $\sim$200 μm, the value reported in Ref. [27]. Interestingly, $\langle N_C \rangle$ increases with V_{FG} and peaks out below 1 for $\nu = 1$ and 3, whereas it exceeds 1 and then levels off below 2 for $\nu = 2$ and 4 [Fig. 3(b)] [34].

To gain insight into the B dependence of λ_{eq} and the even-odd behavior of $\langle N_C \rangle$, we simulated the density profile near the mesa edge by solving the Poisson equation self-consistently within the semiclassical approach taking only Landau quantization into account [35]. In Fig. 4, we compare the density profiles for $\nu = 3$ [Fig. 4(a)] and 4 [Fig. 4(b)] at the same bulk density of 3.65×10^{15} m^{-2}. In both cases, density increases toward the edge, where it drops sharply to zero. Notably, density varies in a stepwise manner due to the formation of compressible and incompressible strips [19]. As the charge equilibration between adjacent edge channels occurs via scattering across the incompressible strip between them [28,36], its width is the important parameter determining the scattering rate. The width is determined by the density gradient at $B = 0$ and the Landau-level energy separation at the strip [19], the latter being the cyclotron and Zeeman

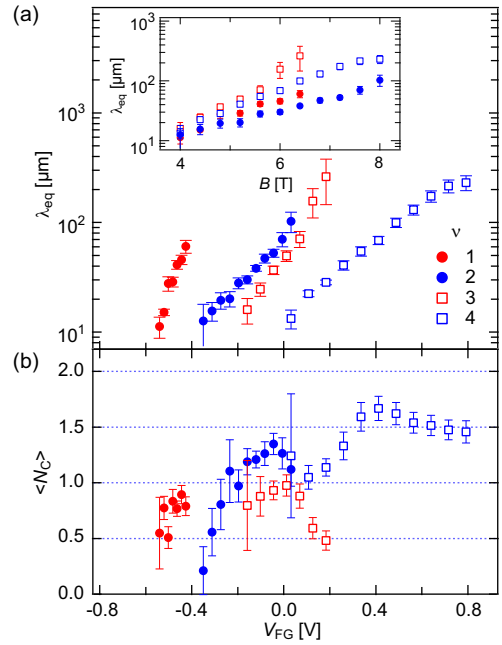

FIG. 3. (a) Equilibration length λ_{eq} and (b) effective number of counterflowing modes $\langle N_C \rangle$ for $\nu = 1$–4 obtained by fitting the g_C vs L_{edge} data, plotted as a function of V_{FG}. The data in (a) are replotted vs B in the inset.

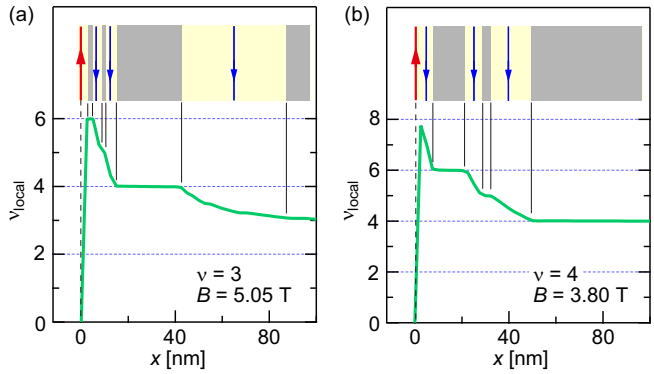

FIG. 4. Simulated density profile, shown as local filling factor $\nu_{\rm local}$, for a bulk electron density of 3.65×10^{15} m^{-2} at magnetic fields corresponding to a bulk filling of (a) $\nu = 3$ and (b) 4. The insets are schematics of the top view near the sample edge. The red (blue) arrows represent forward (counterflowing) edge channels. Incompressible (compressible) regions are shown in gray (yellow).

energy for even and odd local filling ($\nu_{\rm local}$), respectively. Our simulations reveal an important role played by the innermost incompressible strip with even $\nu_{\rm local}$. For odd bulk filling $\nu = 3$, the one with $\nu_{\rm local} = 4$ is the widest [Fig. 4(a)], reflecting the small density gradient (at $B = 0$) and the large cyclotron gap, which then isolates one inner counterflowing channel from all other channels. The outer counterflowing channels are very close to the forward channels and easily equilibrated with them. This explains why only one counterflowing mode can transmit for odd ν. In contrast, for $\nu = 4$, the innermost incompressible strip has $\nu_{\rm local} = 5$, so that it is much narrower, reflecting the small Zeeman gap. Consequently, the widest incompressible strip develops at $\nu_{\rm local} = 6$ [Fig. 4(b)], which isolates two inner counterflowing channels, allowing more than one counterflowing mode to transmit. The B dependence of $\lambda_{\rm eq}$ can be understood in terms of the incompressible-strip width, which we discuss later in detail.

Now we discuss the probe-position and field-direction dependence of the QH effect breakdown presented in Fig. 1. Using the Landauer-Büttiker model, we calculate R_{xx} as a function of $T_{\rm C}$ for the configuration shown in Fig. 5(a). The current-voltage relation can be expressed as $\vec{I} = G_0 \mathbf{M} \vec{V}$, where $\vec{I} = (\ldots, I_i, \ldots)^{\rm T}$ and $\vec{V} = (\ldots, V_i, \ldots)^{\rm T}$ with I_i (V_i) the current (voltage) of the ith contact (i = 1–10) [28]. $\mathbf{M}$ is a matrix with nonzero elements given by

$$M_{i,i} = (\nu + N_{\rm C}) T_{\rm F}^{(i)} + N_{\rm C} T_{\rm C}^{(i-1)},$$
$$M_{i,i+1} = -N_{\rm C} T_{\rm C}^{(i)},$$
$$M_{i,i-1} = -(\nu + N_{\rm C}) T_{\rm F}^{(i-1)}$$

(i mod 10), where $T_{\rm F}^{(i)}$ is the transmission probability of the forward mode on the ith edge. Scattering between forward and counterflowing modes is described by the detailed balance as $(\nu + N_{\rm C})(1 - T_{\rm F}^{(i)}) = N_{\rm C}(1 - T_{\rm C}^{(i)})$. Since all the edges have the same length in the present case, we assume that they share the same $T_{\rm C}$ and $T_{\rm F}$ values. We then solved the above equations with $I_1 = I_{\rm in}$, $I_6 = -I_{\rm in}$, and $V_6 = 0$.

The $T_{\rm C}$ dependence of R_{xx} calculated for $\nu = 2$ and 3 is shown in Fig. 5(b). For these calculations, we took $N_{\rm C} = 1$, for

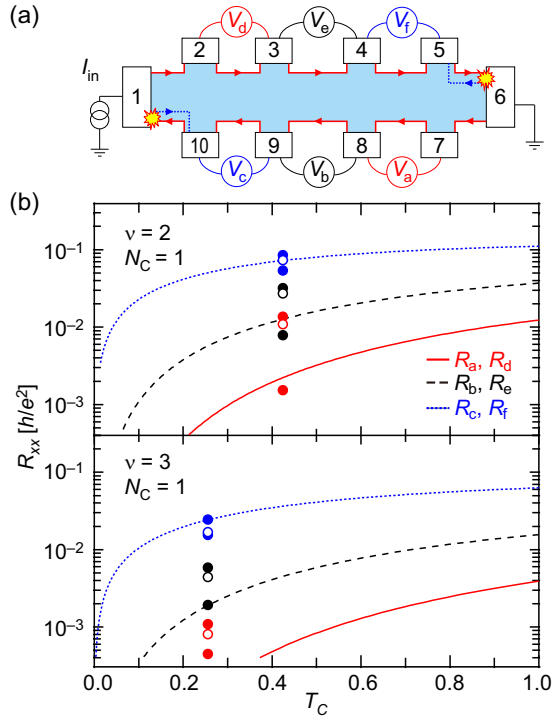

FIG. 5. (a) Configurations used for the calculation of R_{xx}. Yellow markers at the upper-right and lower-left corners represent hot spots. (b) R_{xx} calculated as a function of $T_{\rm C}$ for $\nu = 2$ (upper panel) and 3 (lower panel). R_{xx} values for different probes, $R_\alpha = V_\alpha / I_{\rm in}$ (α = a, ..., f), are shown. Circles are experimental data in Fig. 1, plotted vs $T_{\rm C}$ calculated using the $\lambda_{\rm eq}$ values in Fig. 3(a). Open circles are data for $B < 0$, which are included by using the relation $R_{\rm a}(-B) = R_{\rm c}(B)$.

comparison with the experiment at $V_{\rm FG} = 0$ V [Fig. 3(b)]. The experimental data taken from Fig. 1 are plotted in Fig. 5(b) against $T_{\rm C}[=\exp(-L_{\rm edge}/\lambda_{\rm eq})]$ calculated using $\lambda_{\rm eq}$ for $\nu = 2$ and 3 at $V_{\rm FG} = 0$ V [Fig. 3(a)]. Since the model predicts $R_{\rm a}(-B) = R_{\rm c}(B)$, we included in Fig. 5(b) the data for $B < 0$ using this relation. The calculation reproduces the experimentally observed probe-position dependence, $R_{\rm a} < R_{\rm b} < R_{\rm c}$ for $B > 0$, including the quantitative values. We note that at $V_{\rm FG} = 0$ V the equilibration lengths for $\nu = 2$ and 3 ($\lambda_{\rm eq} \sim 70$ and 50 μm, respectively) are comparable to $L_{\rm edge}$ (=60 μm). Hence, the counterflowing mode, being not fully equilibrated with the forward mode, carries charge to the electrode on the upstream and destroys the QH effect. In contrast, $\lambda_{\rm eq} = 13$ μm for $\nu = 4$ at $V_{\rm FG} = 0$ V is much shorter than $L_{\rm edge}$, implying a nearly full equilibration [37]. This explains why the $\nu = 4$ QH effect is well developed at $V_{\rm FG} = 0$ V, despite the presence of the counterflowing edge channels.

The probe-position and field-direction dependence can be understood intuitively by considering hot spots [38,39]. In the absence of counterflowing modes, the chemical potential of a forward mode just follows that of the current terminal on its upstream. Consequently, all the applied bias between the source and drain contacts is concentrated at the two corners where the forward mode meets the source and drain contacts ("hot spots") [Fig. 5(a)]. In contrast, the chemical potential of the counterflowing mode follows primarily that of the

electrode on its immediate downstream. Therefore, the largest chemical potential difference between the forward mode and counterflowing one occurs near the immediate upstream of the hot spots, yielding the chiral QH breakdown behavior.

We now turn to the B dependence of $\lambda_{\rm eq}$. As shown in Fig. 3(a), $\lambda_{\rm eq}$ increases exponentially with B for both even and odd ν, with nearly the same slope. The inter-edge-channel scattering rate is governed by the wave function overlap between the states involved, which scales as $\propto(d/\ell_B)^{-2}$, where d is the inter-edge distance and $\ell_B = \sqrt{h/2\pi eB}$ is the magnetic length. If d is given by the width of the innermost incompressible strip with even $\nu_{\rm local}$, it is proportional to the square root of the cyclotron energy [19] and hence scales as $\sqrt{B}$. Since $d/\ell_B \propto B$ in this case, one expects $\lambda_{\rm eq}^{-1} \propto \exp[-(B/B_0)^2]$, with B_0 a constant [40]. The experimentally observed dependence, $\lambda_{\rm eq}^{-1} \propto \exp(-B/B_0)$, is different [41], suggesting the relevance of multiple scattering with impurities [42].

Several differences between our results and the previous ones reported for InAs [27] and graphene [28] are worth noting. In Ref. [27], (i) $N_{\rm C}$ was nonzero only for $V_{\rm FG} \lesssim -0.4$ V, and (ii) $N_{\rm C}$ increased linearly up to 6 with decreasing $V_{\rm FG}$. In our experiment, $\langle N_{\rm C}\rangle$ does not show a monotonic $V_{\rm FG}$ dependence, being nonzero for both $V_{\rm FG} < 0$ and $V_{\rm FG} > 0$, with the maximum value peaked out below 2. The chemical properties of the edge [26] and the relative distances of the bulk and edge to the gate [43] may partly account for these differences. However, as our simulations show, the outer counterflowing channels are spatially very close to the forward channels, making it rather unlikely for many of them to transmit [44]. In Ref. [28], despite significant charge accumulation at the edges, QH effects were observed, but at gate voltages shifted from the integer bulk filling. In the edge-state picture, the transport quantization was explained as resulting from strong scattering between forward and counterflowing channels (i.e., short $\lambda_{\rm eq}$) and their isolation from the conductive bulk by the incompressible strip [45]. The microscopic structure of the edge states is nontrivial also in this case, which must be taken into account when making a superconducting junction [46,47].

In summary, we investigated counterflow edge transport in InAs quantum wells in the QH regime and clarified how it equibrates or manifests as a transport anomaly depending on the magnetic field, filling factor, and contact configuration. Our results suggest that counterflowing edge channels can exist in various systems with a sharp edge potential. Thus, even in the integer QH regime, the microscopic structure of the edge states and hence the transport phenomena therein can be more complex than naively expected from the bulk-edge correspondence and should be carefully studied.

The authors thank Yasuhiro Tokura and Masayuki Hashisaka for fruitful discussions and Hiroaki Murofushi for processing the devices. This work was supported by JSPS KAKENHI Grant No. JP15H05854.

[1] B. I. Halperin, Quantized Hall conductance, current-carrying edge states, and the existence of extended states in a two-dimensional disordered potential, Phys. Rev. B **25**, 2185 (1982).

[2] P. Streda, J. Kucera, and A. H. MacDonald, Edge States, Transmission Matrices, and the Hall Resistance, Phys. Rev. Lett. **59**, 1973 (1987).

[3] M. Büttiker, Absence of backscattering in the quantum Hall effect in multiprobe conductors, Phys. Rev. B **38**, 9375 (1988).

[4] C. L. Kane and E. J. Mele, Quantum Spin Hall Effect in Graphene, Phys. Rev. Lett. **95**, 226801 (2005).

[5] C. L. Kane and E. J. Mele, Z_2 Topological Order and the Quantum Spin Hall Effect, Phys. Rev. Lett. **95**, 146802 (2005).

[6] N. H. Lindner, E. Berg, G. Refael, and A. Stern, Fractionalizing Majorana Fermions: Non-Abelian Statistics on the Edges of Abelian Quantum Hall States, Phys. Rev. X **2**, 041002 (2012).

[7] A. Vaezi, Fractional topological superconductor with fractionalized Majorana fermions, Phys. Rev. B **87**, 035132 (2013).

[8] D. J. Clarke, J. Alicea, and K. Shtengel, Exotic non-Abelian anyons from conventional fractional quantum Hall states, Nat. Commun. **4**, 1348 (2013).

[9] R. S. K. Mong, D. J. Clarke, J. Alicea, N. H. Lindner, P. Fendley, C. Nayak, Y. Oreg, A. Stern, E. Berg, K. Shtengel, and M. P. A. Fisher, Universal Topological Quantum Computation from a Superconductor-Abelian Quantum Hall Heterostructure, Phys. Rev. X **4**, 011036 (2014).

[10] D. J. Clarke, J. Alicea, and K. Shtengel, Exotic circuit elements from zero-modes in hybrid superconductor-quantum-Hall systems, Nat. Phys. **10**, 877 (2014).

[11] J. Alicea, New directions in the pursuit of Majorana fermions in solid state systems, Rep. Prog. Phys. **75**, 076501 (2012).

[12] M. Leijnse and K. Flensberg, Introduction to topological superconductivity and Majorana fermions, Semicond. Sci. Technol. **27**, 124003 (2012).

[13] I. Knez, R. R. Du, and G. Sullivan, Andreev Reflection of Helical Edge Modes in InAs/GaSb Quantum Spin Hall Insulator, Phys. Rev. Lett. **109**, 186603 (2012).

[14] V. S. Pribiag, A. J. A. A. Beukman, F. Qu, M. C. Cassidy, C. Charpentier, W. Wegscheider, and L. P. Kouwenhoven, Edge-mode superconductivity in a two-dimensional topological insulator, Nat. Nanotechnol. **10**, 593 (2015).

[15] F. K. de Vries, T. Timmerman, V. P. Ostroukh, J. van Veen, A. J. A. Beukman, F. Qu, M. Wimmer, B.-M. Nguyen, A. A. Kiselev, W. Yi, M. Sokolich, M. J. Manfra, C. M. Marcus, and L. P. Kouwenhoven, h/e Superconducting Quantum Interference through Trivial Edge States in InAs, Phys. Rev. Lett. **120**, 047702 (2018).

[16] T. Tschirky, S. Mueller, Ch. A. Lehner, S. Fält, T. Ihn, K. Ensslin, and W. Wegscheider, Scattering mechanisms of highest-mobility InAs/Al_xGa_{1-x}Sb quantum wells, Phys. Rev. B **95**, 115304 (2017).

[17] C. Thomas, A. T. Hatke, A. Tuaz, R. Kallaher, T. Wu, T. Wang, R. E. Diaz, G. C. Gardner, M. A. Capano, and M. J. Manfra, High-mobility InAs 2DEGs on GaSb substrates: A platform

for mesoscopic quantum transport, Phys. Rev. Mater. **2**, 104602 (2018).

[18] M. K. Ma, Md. Shafayat Hossain, K. A. Villegas Rosales, H. Deng, T. Tschirky, W. Wegscheider, and M. Shayegan, Observation of fractional quantum Hall effect in an InAs quantum well, Phys. Rev. B **96**, 241301(R) (2017).

[19] D. B. Chklovskii, B. I. Shklovskii, and L. I. Glazman, Electrostatics of edge channels, Phys. Rev. B **46**, 4026 (1992).

[20] In the fractional QH regime, electron correlation can lead to an edge state with a nonmonotonic density profile and counterflowing modes, which is outside the scope of this work. See Ref. [48] and references therein.

[21] J. R. Waldrop, Schottky-barrier height of ideal metal contacts to GaAs, Appl. Phys. Lett. **44**, 1002 (1984).

[22] M. Noguchi, K. Hirakawa, and T. Ikoma, Intrinsic Electron Accumulation Layers on Reconstructed Clean InAs(100) Surfaces, Phys. Rev. Lett. **66**, 2243 (1991).

[23] F. Nichele, H. J. Suominen, M. Kjaergaard, C. M. Marcus, E. Sajadi, J. A. Folk, F. Qu, A. J. A. Beukman, F. K. de Vries, J. van Veen, S. Nadj-Perge, L. P. Kouwenhoven, B. M. Nguyen, A. A. Kiselev, W. Yi, M. Sokolich, M. J. Manfra, E. M. Spanton, and K. A. Moler, Edge transport in the trivial phase of InAs/GaSb, New J. Phys. **18**, 083005 (2016).

[24] B.-M. Nguyen, A. A. Kiselev, R. Noah, W. Yi, F. Qu, A. J. A. Beukman, F. K. de Vries, J. van Veen, S. Nadj-Perge, L. P. Kouwenhoven, M. Kjaergaard, H. J. Suominen, F. Nichele, C. M. Marcus, M. J. Manfra, and M. Sokolich, Decoupling Edge Versus Bulk Conductance in the Trivial Regime of an InAs/GaSb Double Quantum Well Using Corbino Ring Geometry, Phys. Rev. Lett. **117**, 077701 (2016).

[25] S. Mueller, C. Mittag, T. Tschirky, C. Charpentier, W. Wegscheider, K. Ensslin, and T. Ihn, Edge transport in InAs and InAs/GaSb quantum wells, Phys. Rev. B **96**, 075406 (2017).

[26] C. Mittag, M. Karalic, S. Mueller, T. Tschirky, W. Wegscheider, O. Nazarenko, M. V. Kovalenko, T. Ihn, and K. Ensslin, Passivation of edge states in etched InAs sidewalls, Appl. Phys. Lett. **111**, 082101 (2017).

[27] B. J. van Wees, G. I. Meijer, J. J. Kuipers, T. M. Klapwijk, W. van de Graaf, and G. Borghs, Breakdown of the quantum Hall effect in InAs/AlSb quantum wells due to counterflowing edge channels, Phys. Rev. B **51**, 7973 (1995).

[28] Y. T. Cui, B. Wen, E. Y. Ma, G. Diankov, Z. Han, F. Amet, T. Taniguchi, K. Watanabe, D. Goldhaber-Gordon, C. R. Dean, and Z. X. Shen, Unconventional Correlation between Quantum Hall Transport Quantization and Bulk State Filling in Gated Graphene Devices, Phys. Rev. Lett. **117**, 186601 (2016).

[29] P. G. Silvestrov and K. B. Efetov, Charge accumulation at the boundaries of a graphene strip induced by a gate voltage: Electrostatic approach, Phys. Rev. B **77**, 155436 (2008).

[30] The etching was done in two steps. First, the upper antimonide layers were removed with a 1:5 solution of NH_4OH (30%) and H_2O, and then the InAs and lower antimonide layers were etched with $H_3PO_4 : H_2O_2 : H_2O$ (=1:1:15).

[31] A detailed balance requires $(\nu + N_C)(1 - T_F^{(i)}) = N_C(1 - T_C^{(i)})$ for each edge, where $T_F^{(i)}$ is the transmission probability of the forward modes on the ith edge. By solving this for $T_F^{(i)}$ and plugging it into $g_F^{(i)} = (\nu + N_C)T_F^{(i)}$, we have $g_F^{(i)} = \nu + N_C T_C^{(i)} = \nu + g_C^{(i)}$.

[32] The fact that g_C decreases as V_{FG} is slightly lowered from integer ν is consistent with the conjecture that the electron density in the vicinity of the mesa edge is higher than that in the bulk.

[33] For $\nu = 1$ and 3, only data for $B \leqslant 6.4$ T, for which good fitting with the exponential function was obtained, are included.

[34] Note that $\langle N_C \rangle$ is the effective number of counterflowing modes, not the actual number of counterflowing edge channels determined by the density profile and magnetic field. In addition, disorder may affect the value of $\langle N_C \rangle$; potential fluctuation near the edge may cause N_C to vary between 2 and 1 (or between 1 and 0) along the edge, making $\langle N_C \rangle$ non-integer.

[35] The Poisson equation was solved in the two-dimensional plane perpendicular to the sample edge. We employed a simplified geometry, with a 400-nm-wide zero-thickness channel surrounded by 100-nm-thick insulator with a dielectric constant of $\varepsilon_r = 15$ and a metallic gate in all four directions. An effective mass of $0.026m_e$ and g-factor of 10 were used to calculate the energies of the Landau levels, which were then broadened by a Gaussian function with $\sigma = 0.3$ meV. Finite-temperature effects were not included. A fixed line charge of $-0.05e$ nm^{-1} along the channel edge was assumed to obtain realistic density profiles.

[36] B. W. Alphenaar, P. L. McEuen, R. G. Wheeler, and R. N. Sacks, Selective Equilibration Among the Current-Carrying States in the Quantum Hall Regime, Phys. Rev. Lett. **64**, 677 (1990).

[37] Indeed, $T_c = 0.01$ for $\nu = 4$ yields $R_{xx} \leqslant 6 \times 10^{-4}(h/e^2)$.

[38] U. Klaß, W. Dietsche, K. von Klitzing, and K. Ploog, Imaging of the dissipation in quantum-Hall-effect experiments, Z. Phys. B: Codens. Matter **82**, 351, (1991)

[39] S. Komiyama, H. Sakuma, K. Ikushima, and K. Hirakawa, Electron temperature of hot spots in quantum Hall conductors, Phys. Rev. B **73**, 045333 (2006).

[40] T. Martin and S. Feng, Suppression of Scattering in Electron Transport in Mesoscopic Quantum Hall Systems, Phys. Rev. Lett. **64**, 1971 (1990).

[41] A similar exponential B dependence is known for copropagating edge channels in GaAs, which was observed when B was varied around integer fillings at a fixed density and explained by the increase in the inter-edge distance with decreasing ν [19]. In the present case, g_C drops more quickly with L_{edge} as ν is slightly reduced from integer values [Fig. 2(c)], suggesting that the inter-edge distance becomes smaller with decreasing ν.

[42] T. Martin and S. Feng, Suppression of inter-edge-state equilibration due to multiple scattering with impurities, Phys. Rev. B **44**, 9084 (1991).

[43] Although not shown here, our experiments suggest that the edge potential depends also on other factors such as the quantum well thickness, distance from the surface, and the history of gate sweep, which will be reported separately.

[44] It is not clear whether the large N_C values found in Ref. [27] originate from the various assumptions made in the analysis. Our approach, in which one directly measures the counterflowing charge current for each individual edge, provides reliable values for $\langle N_C \rangle$ and T_C.

[45] This happens only when the incompressible strip isolates the bulk from Ohmic contacts. Whether this happens or not depends on the density profile near the Ohmic contacts [49].

[46] F. Amet, C. T. Ke, I. V. Borzenets, J. Wang, K. Watanabe, T. Taniguchi, R. S. Deacon, M. Yamamoto,

Y. Bomze, S. Tarucha, and G. Finkelstein, Supercurrent in the quantum Hall regime, Science **352**, 966 (2016).

[47] G.-H. Lee, K.-F. Huang, D. K. Efetov, D. S. Wei, S. Hart, T. Taniguchi, K. Watanabe, A. Yacoby, and P. Kim, Inducing superconducting correlation in quantum Hall edge states, Nat. Phys. **13**, 693 (2017).

[48] F. Lafont, A. Rosenblatt, M. Heiblum, and V. Umansky, Counter-propagating charge transport in the quantum Hall effect regime, Science **363**, 54 (2019).

[49] F. Dahlem, E. Ahlswede, J. Weis, and K. v. Klitzing, Cryogenic scanning force microscopy of quantum Hall samples: Adiabatic transport originating in anisotropic depletion at contact interfaces, Phys. Rev. B **82**, 121305 (2010).